Nigerian Journal of Physics (NJP)
ISSN online: 3027-0936
ISSN print: 1595-0611
DOI: https://doi.org/10.62292/njp.v35(S).2026.783
Volume 35(S), November 2026

Synthesis and Characterization of Zinc Tin-Oxide (Zn–Sn–O) Thin Films for Solar Cell Application

[1]Mohammed Abdullahi, [1]Pascal Timtere, and [1]Yusuf Dahiru

[1]Department of Physics, School of Physical Sciences, Modibbo Adama University, Yola, Nigeria

*Corresponding Author's Email: mohamabdulmed@gmail.com Phone No.: +2349070105058

Keywords:
Zinc tin oxide;
Sn-doped ZnO;
Thin films;
X-ray diffraction;
Electrical conductivity;
Optical band gap

Submitted: 16/10/2026

Accepted: 3/11/2026

Published: 14/11/2026

ABSTRACT

This study investigates the influence of tin (Sn) doping on the structural, microstructural, electrical, and optical properties of $Zn_{1-x}Sn_xO$ nanoparticles at four dopant concentrations: x = 0.000, 0.001, 0.003, and 0.005, designated as Samples A, B, C, and D, respectively. X-ray diffraction (XRD) analysis confirmed that all samples retained the hexagonal wurtzite ZnO structure (JCPDS 36-1451) with no detectable secondary SnO_2 phases, indicating successful substitutional incorporation of Sn into the ZnO lattice. The crystallite size varied non-monotonically, increasing from 18.34 nm (undoped) to a maximum of 20.47 nm at x = 0.003, while microstrain and dislocation density reached their minimum values at the same composition. Scanning electron microscopy (SEM) revealed progressive modifications in particle morphology and agglomeration with increasing Sn content, and energy-dispersive X-ray spectroscopy (EDS) confirmed the presence and systematic increase of Sn in the doped samples. Electrical characterization showed predominantly ohmic current–voltage behaviour for all samples. The electrical conductivity increased from approximately 26 S cm^{-1} for the undoped sample to a maximum of approximately 51 S cm^{-1} at x = 0.003, before declining to approximately 42 S cm^{-1} at x = 0.005, with resistivity following the inverse trend. This non-monotonic behaviour was attributed to the competing effects of Sn^{4+} donor-related carrier generation and ionized impurity scattering at higher doping levels. Optical transmittance spectra showed that all films maintained greater than 90% visible transmittance with a sharp ultraviolet absorption edge. Tauc analysis yielded optical band gaps of 3.30, 3.32, 3.35, and 3.32 eV for Samples A–D, respectively, with the maximum blue-shift of 0.05 eV at x = 0.003 attributed to the Burstein–Moss effect. The slight band-gap contraction at x = 0.005 was associated with the onset of band-gap renormalization and Urbach band-tailing. The coherence between structural and optical data identifies x = 0.003 as the optimum Sn doping level, combining the best crystalline quality, highest electrical conductivity, and maximum band-gap widening, making it a promising composition for transparent-conductor and optoelectronic applications.

INTRODUCTION

Growing concerns about fossil-fuel depletion and the environmental effects of carbon-based energy systems have increased interest in renewable energy sources. Solar energy offers a renewable route to electricity generation with lower direct emissions than fossil-fuel systems. The performance and cost of photovoltaic (PV) systems depend partly on the properties of the materials used in their construction. Recent research has focused on using oxide semiconductors in thin-film solar cells because they are plentiful, chemically stable, and may offer high optical transparency (Green, 2020).

Zinc–tin oxide (ZTO) has attracted attention as a ternary oxide for photovoltaic applications. It is recognized for its combination of good electrical conductivity from tin oxide (SnO_2) and high transparency from zinc oxide (ZnO), which makes it appropriate for use as a transparent conducting oxide (TCO) layer in solar cells.

The adjustable bandgap of ZTO, usually between 3.2 and 3.9 eV, offers a significant benefit for optoelectronic uses, particularly in improving light absorption and charge movement in solar cells (Chopra & Major, 2019). In ternary oxides such as ZTO, changing the cation composition and deposition conditions provides a way to adjust film properties. This positions them as a practical substitute for traditional materials such as Indium Tin Oxide (ITO), which, although commonly used, is costly and not very abundant. ZTO films can be produced using several methods, including chemical spray pyrolysis, RF magnetron sputtering, sol-gel spin coating, and pulsed laser deposition. Each technique impacts the film's micro-structure, crystallinity, optical transparency, and electrical conductivity, which subsequently affects the performance of the solar cell (Okoye et al., 2021).

The development of efficient thin films also requires detailed characterization of their structural, optical, and electrical properties. These properties determine the film's functionality as a component in photovoltaic devices. For example, the crystallite size, surface roughness, bandgap energy, transmittance, and carrier mobility are critical parameters that must be optimized to achieve high-efficiency solar cells (Kim & Lee, 2022). Understanding the relationship between preparation conditions and material properties is therefore essential to improve the performance and stability of solar devices.

In countries like Nigeria, there is an immediate need for tailored solutions to address energy shortages. Using ZTO thin films in solar technology offers an affordable and effective solution to this issue. Areas such as Biu Local Government Area in Borno State, which experience inadequate electricity infrastructure, could significantly gain from the implementation of affordable solar energy systems produced locally. Research in these areas helps expand global knowledge-based and promotes technological progress and energy independence in the region (Adelakun et al., 2020).

This study examines the synthesis and characterization of ZTO thin films for potential solar-cell applications. The ultimate aim is to optimize the material's optical and electrical properties for enhanced solar energy conversion. Through this, the research seeks to contribute meaningfully to the development of affordable and efficient renewable energy technologies tailored to local environmental and economic conditions.

Conventional unitary and binary thin films used in solar cell technologies often face significant limitations, including sub-optimal band gap values, narrow absorption spectra, low electrical conductivity, and limited control over optical and structural properties (Avasthi, 2016). These deficiencies hinder the overall efficiency and adaptability of solar energy devices, especially as the demand for low-cost, high-performance, and environmentally friendly photovoltaic materials continues to grow.

To overcome these challenges, research has increasingly turned to ternary oxide materials, such as ZTO, which offer enhanced tunability of optical and electrical properties through compositional control. The unique combination of zinc and tin oxides enables a wider range of band gap engineering, improved absorption characteristics, higher carrier mobility, and more stable crystal structures. However, despite their promising attributes, the synthesis and detailed characterization of ZTO thin films remain under explored, particularly in terms of optimizing their performance for solar cell applications.

This study, therefore, seeks to synthesize and characterize ZTO thin films, with a focus on evaluating their structural, optical, and electrical properties to assess their suitability for efficient solar energy conversion. By tailoring the composition and processing conditions, the research aims to contribute to the development of cost-effective, high-efficiency thin-film solar cells based on ternary oxide systems (Fazal *et al.*, 2022).

The study aimed to synthesize and characterize zinc–tin oxide (ZTO) thin films and assess their potential suitability for solar-cell applications. The aim will be achieved with the following objectives to:

i. Determine the optical properties of the ZTO thin films including transmittance, reflectance
ii. Determine the electrical properties of the ZTO thin film (conductivity, carrier mobility, and Carrier Concentration)
iii. Analyze the structural properties (crystallinity; grain size or morphology) using SEM, X-ray diffraction
iv. Examine the surface properties (Surface roughness, and surface defects) – Atomic force microscopy (AFM)

The synthesis and characterization of ZTO serve as an important area of the research in solid state physics. This is because the ternary thin films have potential to revolutionize the fabrication of both electronic and optoelectronic components of electrical devices due to their synergy and tunability which arises from their constituents which consist of three different elements as opposed to unitary and binary thin films.

The study limited to fabrication of ZTO thin films, characterization and the determination of state properties of the fabricated thin films. The study further investigated the potential application of the fabricated ZTO thin films as functional layers in solar cells and evaluate their suitability for enhancing solar-cell performance

MATERIALS AND METHODS

Data and Modelling Framework

Materials

The materials and chemical reagents required for the synthesis of zinc–tin oxide (ZTO) thin films and fabrication of the solar-cell devices are shown in table 3.1

Table 3.1: Materials and Chemicals

S/N	Material	Quantity	Specification
1	$ZnCl_2$	1.39g	Reagent grade
2	$SnCl_2$	3,50g	Reagent grade
3	Distilled Water	5000mL	Pure water, chemical grade
4	Sieve	1	Mesh size as per requirement
5	Whatman Filter Paper no.1	1 pack	Grade 1
6	Beakers	6	Various sizes, borosilicate glass
7	Conical Flasks	10	Various sizes, borosilicate glass
8	Funnel	1	Standard size
9	Glass subtractes	1	15 mm by 22 mm
10	Refrigerator	1	Laboratory grade
11	Aluminum Foil Paper	1 roll	Laboratory grade
12	Magnetic Stirrer	1	With stir bar
13	Digital Weighing Balance	1	Precision, 0.01 g accuracy
14	Single Hotplate	1	Adjustable temperature
15	Spatula	1	Stainless steel
16	Silver Crest Blender	1	High speed
17	Masking Tape	1 roll	Standard size
18	Hand Gloves	1 box	Nitrile, normal sizes
19	Face Mask	1 box	Disposable, normal sizes
20	Spin Coater	1	3 mm thickness, 10 mm diameter
21	Ethanol	50mL	Reagent grade
22	Centrifuge Machine	1	4000rpm
23	Scanning Electron Microscopy	1	SEM, high-resolution imaging
24	X-ray Diffraction	1	XRD, phase analysis
25		1	

Methods

The research involve the synthesis of ZTO thin films using the sol-gel spin-coating technique, followed by structural, optical, morphological, and electrical characterization. The optimized ZTO films will subsequently be incorporated into solar-cell devices to evaluate their suitability for photovoltaic application.

Substrate Cleaning

Glass substrates measuring approximately 15 mm × 20 mm will be used for the deposition of ZTO thin films. The substrates will first be washed thoroughly with laboratory detergent and rinsed with distilled water to remove dust and surface contaminants. The substrates will subsequently be ultrasonically cleaned in ethanol, and for approximately 10 minutes in each solvent. After cleaning, the substrates will be rinsed with distilled water and dried using clean compressed air. The substrates will then be heated at approximately 100 °C for 20–30 minutes to remove residual moisture.

The cleaned substrates will be stored in clean, covered containers prior to film deposition. Proper substrate cleaning will be maintained for all samples to ensure good film adhesion and minimize surface-related defects.

Preparation of ZTO Precursor Solution

ZTO precursor solutions will be prepared from $ZnCl_2$ and $SnCl_4 \cdot 5H_2O$ using a 1:1 Zn:Sn molar ratio and 0.20 M concentration. The precursors will be dissolved separately, combined, and stirred at 60 °C for 2 h to obtain a homogeneous solution. The solution was then aged for 24 h at room temperature in a sealed container and visually inspected to ensure clarity and the absence of precipitates before spin coating.

Deposition and Annealing of ZTO Thin Films

ZTO thin films will be deposited on cleaned glass substrates using the spin-coating technique. Approximately 30–50 µL of the precursor solution will be applied to each substrate and spun at 3,500 rpm for 30 s. The coated substrates will be pre-heated at 100–150 °C for 10–15 min to remove residual solvent. This process will be repeated three times to obtain uniform films of the desired thickness.

The coated films will subsequently be annealed in a programmable furnace at 400, 450, and 500 °C for 1 h, while maintaining a constant number of coating cycles for all samples. After annealing, the films will be allowed to cool gradually inside the furnace. The effect

of annealing temperature on the structural, optical, morphological, and electrical properties of the ZTO thin films will then be evaluated.

Film Characterization

The synthesized ZTO thin films will be characterized to determine their structural, optical, morphological, compositional, and electrical properties.

X-Ray Diffraction (XRD)

X-ray diffraction will be used to determine the crystalline structure, phase composition, preferred orientation, and crystallinity of the ZTO films. The diffraction patterns will be obtained using Cu-Kα radiation with a wavelength of approximately 1.5406 Å over an appropriate 2θ range, preferably 20–80°. The average crystallite size will be estimated using the Scherrer equation:

$$D = \frac{k\lambda}{\beta \cos\theta} \quad 3.1$$

where D is the crystallite size, K is the shape factor, λ is the wavelength of the X-ray radiation, β is the full width at half maximum (FWHM), and θ is the Bragg angle.

UV-Visible Spectrophotometry

The optical properties of the films will be determined using a UV-Visible spectrophotometer. The optical transmittance and absorbance will be measured over approximately 300–900 nm. The optical band gap estimated using the Tauc relation:

$$(\alpha h\nu)n = A(h\nu - Eg) \quad 3.2$$

where α is the absorption coefficient, hν is the photon energy, Eg is the optical band gap, A is a constant, and n represents the nature of the electronic transition.

Scanning Electron Microscopy (SEM)

SEM will be used to examine the surface morphology of the ZTO films. The analysis will provide information on grain morphology, surface uniformity, grain size, pores, cracks, pinholes, and other surface defects. Where cross-sectional SEM analysis is available, it will also be used to estimate the thickness of the deposited films.

Energy-Dispersive X-Ray Spectroscopy (EDS)

EDS coupled with SEM will be employed to determine the elemental composition of the films. The presence of zinc, tin, and oxygen will be confirmed, and the relative Zn/Sn composition will be estimated.

Electrical Characterization

The electrical properties of the films will be measured using a four-point probe system. The sheet resistance will be measured at different positions on each film to evaluate electrical uniformity. The resistivity will be calculated using:

$$\rho = Rst \quad 3.3$$

where ρ is the electrical resistivity, Rs is the sheet resistance, and t is the film thickness. The electrical conductivity will be calculated as:

$$\sigma = 1\rho \quad 3.4$$

where σ is the electrical conductivity.

Solar Cell Fabrication

The ZTO thin film with the optimum properties will be selected for solar-cell fabrication. The device will use the Glass/FTO/ZTO/Perovskite/HTL/Metal structure, with ZTO serving as the electron-transport layer. The cleaned FTO substrate will be coated with the optimized ZTO film, followed by deposition of the perovskite absorber, HTL, and metal electrode. The active area of each device will be defined and kept constant.

Solar Cell Characterization

The fabricated solar cells will be tested under simulated sunlight, and their open-circuit voltage (**Voc),** short-circuit current density (**Jsc),** fill factor (**FF),** and power-conversion efficiency (PCE).

The fill factor will be calculated using:

$$FF = VmpJmp\ /VocJsc \quad 3.5$$

The power-conversion efficiency will be calculated from:

$$\eta = \frac{VocIscFF}{Pin} \times 100\% \quad 3.6$$

where Pin is the incident solar power density

RESULTS AND DISCUSSION

Structural Properties of Sn doped ZnO Nanoparticles

The X-ray diffraction patterns of $Zn_{1-x}Sn_xO$ samples with x=0.000, 0.001, 0.003 and 0.005 are presented in Figure 4.1. The XRD patterns of $Zn_{1-x}Sn_xO$ samples A–D confirm that all samples retain the characteristic hexagonal wurtzite structure of ZnO. The principal diffraction peaks observed at approximately 2θ=31.84°, 34.52°, 36.28°, 47.5°, 56.65° and 62.87° can be indexed to the (100), (002), (101), (102), (110), (103) and (200) planes, respectively. These reflections agree well with the standard wurtzite ZnO structure (JCPDS 36-1451). The (101) reflection is the most intense peak, indicating preferential orientation along this plane. No distinct secondary peaks attributable to SnO_2 or other impurity phases are evident, suggesting that the low concentrations of Sn do not significantly alter the ZnO wurtzite phase and that Sn is likely incorporated into the ZnO lattice within the detection limit of XRD. The increase in overall peak intensity from sample A to D also suggests an improvement in the apparent crystallinity and/or the amount of well-oriented crystalline material with increasing Sn concentration.

The differences in peak intensities and profiles among samples A–D indicate that Sn incorporation influences the structural ordering and crystal-growth behaviour of ZnO. Because the Sn concentrations are very low, any shift in peak position is expected to be subtle; nevertheless, substitution of Zn by Sn can introduce lattice distortion, strain and point defects due to differences in the charge state and local coordination of the dopant. The preservation of the same diffraction pattern across all compositions demonstrates that the fundamental ZnO crystal structure remains stable up to x=0.005.

The present results are consistent with recent reports on Sn-doped ZnO, although the effect of Sn concentration on crystallinity can depend strongly on the synthesis method and dopant level. Munna et al., (2023) reported retention of the hexagonal ZnO structure, absence of secondary SnO_2 phases and preferential orientation along the (101) plane after Sn doping, while observing changes in peak intensity, FWHM, crystallite size and lattice strain with increasing Sn content. More recently, Arif et al., (2025) also confirmed that Sn doping preserves the wurtzite ZnO phase without impurity peaks but can modify peak positions, crystallinity and defect-related lattice strain. Thus, the present XRD results support the conclusion that low-level Sn doping modifies the crystallographic quality and lattice characteristics of ZnO without causing a structural phase transformation.

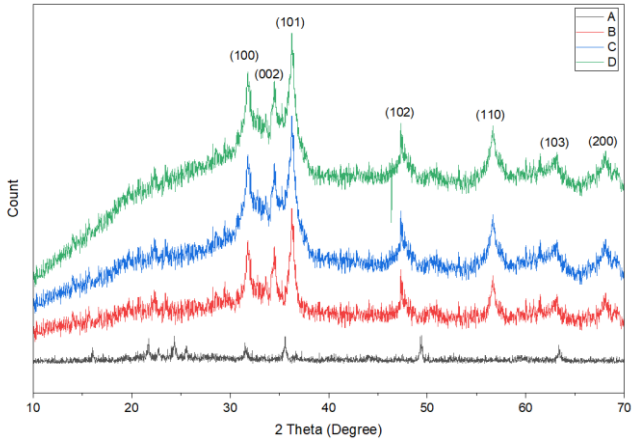


Figure 1: XRD spectra of Sn doped ZnO

Sample A represents undoped ZnO and provides the reference structure. The diffraction peaks are characteristic of hexagonal wurtzite ZnO, with the (101) reflection appearing as the dominant peak. This agrees with reports in which the (101) plane is the preferred growth orientation of ZnO nanostructures. In sample B, the same ZnO reflections remain visible. There is no obvious additional crystalline phase. The small change in peak profile relative to A can be attributed to the initial incorporation of Sn into the ZnO lattice and the resulting local structural distortion/defect modification.

The wurtzite structure is still maintained in sample C. The changes in peak intensity and broadening compared with A and B indicate that Sn is influencing the crystallization process. At this concentration, Sn may act as a lattice perturbation and modify nucleation and grain growth. Importantly, the absence of distinct SnO_2 reflections suggests that the Sn concentration remains below the level required to produce a readily detectable separate crystalline SnO_2 phase.

Sample D continues to exhibit the same ZnO wurtzite reflections, with particularly clear (100), (002), (101), (102), (110), (103) and (200) peaks. Thus, increasing the Sn content to 0.5 at.% does not destroy the ZnO host lattice. The broadening/profile changes visible in the pattern suggest increasing structural disorder or changes in crystallite dimensions.

The structural parameters extracted from the X-ray diffraction patterns of the Sn-doped ZnO nanoparticles are collected in Table 4.1. For each nanoparticles the diffraction angles of the (100) and (101) reflections, the full width at half maximum (FWHM, β_{101}) of the (101) peak, the lattice parameters a and c, the axial ratio c/a, the interplanar spacing d, the crystallite size D (Scherrer equation), the microstrain ε and the dislocation density δ are listed.

Table 4.1: Structural parameters of the Sn-doped ZnO nanoparticles

Sample ID	$2\theta_{100}$	$2\theta_{101}$	$\beta(°)$	**Lattice Parameters**	**c/a**	d(Å)	**D (nm)**	ε **(%)**	**dislocation density,** δ

	(°)	(°)		**a** (Å)	**c** (Å)					**(nm⁻²)**
A	32.240	36.592	0.456	3.221	5.160	1.602	2.584	18.34	0.602	2.973×10^{-3}
B	31.807	36.290	0.447	3.246	5.204	1.603	2.478	18.69	0.595	2.862×10^{-3}
C	31.823	36.297	0.408	3.244	5.200	1.603	2.473	20.47	0.544	2.387×10^{-3}
D	30.861	36.967	0.424	3.243	5.192	1.601	2.430	19.75	0.554	2.563×10^{-3}

All four nanoparticles exhibit the (100) and (101) reflections of the hexagonal wurtzite ZnO structure, with an axial ratio c/a of 1.601–1.603 for every sample, confirming that the wurtzite lattice is retained and that no secondary Sn-oxide phase is detected within the resolution of the measurement. The lattice parameters (a ≈ 3.22–3.25 Å, c ≈ 5.16–5.20 Å) are close to the standard bulk ZnO values (a = 3.2498 Å, c = 5.2066 Å).

The crystallite size varies non-monotonically with Sn content: it increases from 18.34 nm (A) to a maximum of 20.47 nm at a Sn content of 0.003 (C), then decreases to 19.75 nm at 0.005 (D). This trend mirrors the FWHM of the (101) peak, which is narrowest for sample C (0.408°) and broadest for the undoped sample A (0.456°), in accordance with the inverse relationship between crystallite size and peak broadening in the Scherrer analysis. The microstrain (ε) and dislocation density (δ) follow the opposite trend, both reaching their minima for sample C (ε = 0.544 %, δ = 2.387×10^{-3} nm^{-2}) and their maxima for the undoped sample A (ε = 0.602 %, δ = 2.973×10^{-3} nm^{-2}). A shift of the (100) reflection toward lower diffraction angles upon doping (from 32.240° in A to ~31.8° in B and C, and 30.861° in D) accompanies a small expansion of the lattice parameter, a, relative to the undoped nanoparticles.

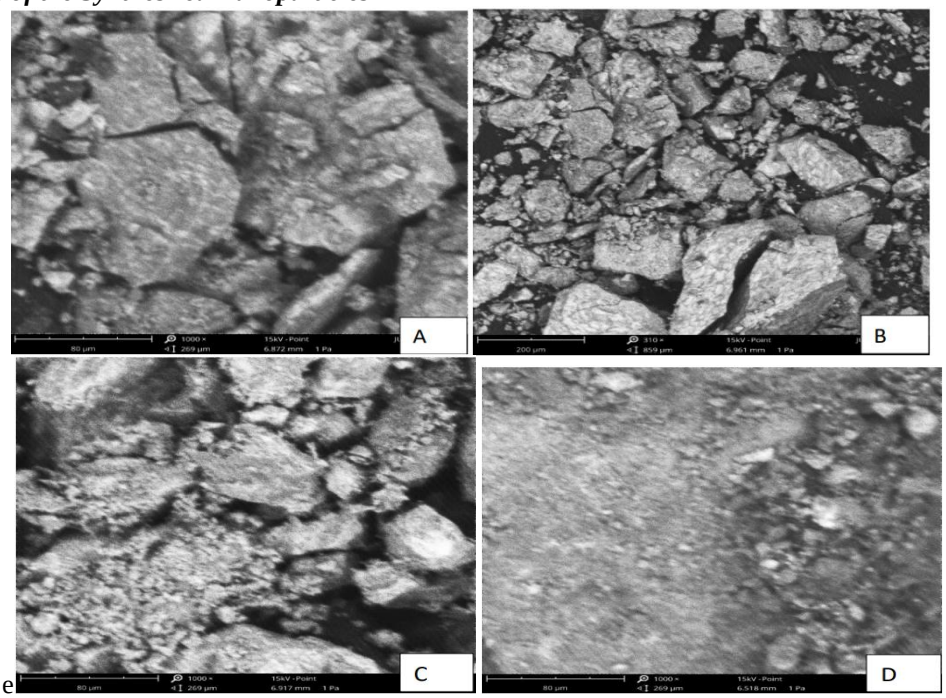
The retention of the wurtzite structure and the near-constant c/a ratio (≈1.60) across all compositions indicate that tin is incorporated substitutionally into the ZnO lattice without disrupting the host structure or forming a detectable secondary phase. The shift of the (100) peak to lower angles and the accompanying expansion of the lattice parameter, a, reflect a modification of the lattice on doping. Although the ionic radius of Sn^{4+} smaller than that of Zn^{2+}, the observed lattice expansion is commonly reported for Sn-doped ZnO and is attributed to the local lattice distortion and electrostatic strain introduced by the higher-valent Sn^{4+} substituting the divalent Zn^{2+} site, together with the possible occupation of interstitial sites; the resulting charge imbalance and defect accommodation expand the cell (Chahmat et al., 2012; Munna et al., 2023).

The most significant structural result is the non-monotonic evolution of crystallinity with doping. The simultaneous maximisation of crystallite size and minimization of microstrain and dislocation density at a Sn content of 0.003 (sample C) shows that this composition has the best crystalline quality of the series. At low-to-intermediate doping, dilute Sn^{4+} ions can promote grain growth and relieve intrinsic strain, improving crystallinity; beyond the optimum (sample D, 0.005), the increasing dopant concentration approaches the solubility limit, enhancing lattice disorder, grain-boundary scattering and defect formation, which reduces the crystallite size and raises the strain and dislocation density again. This non-monotonic behaviour is widely reported for Sn-doped ZnO and other doped ZnO systems (Chahmat et al., 2012; Russiarani & Ramesh Kumar, 2023; Yildirimcan et al., 2024).

The inverse correlation between crystallite size (D) and both microstrain (ε) and dislocation density (δ) is the expected signature of X-ray line-profile analysis: larger, more perfect crystallites present fewer grain boundaries and defects, so the strain-broadening and dislocation terms are correspondingly smaller (Munna et al., 2023). Importantly, these structural trends are fully consistent with the optical results obtained in this work: sample C, which exhibits the largest crystallite size and the lowest defect density, also displays the widest optical band gap (3.35 eV) in the Tauc analysis, whereas the undoped nanoparticles A, with the smallest crystallites and highest defect density, shows the narrowest gap (3.30 eV). The coherence between the structural and optical data strengthens the interpretation that a Sn content of 0.003 represents the optimum doping level, combining the best crystalline quality with the maximum band-gap widening.

Microstructural Properties of synthesized nanoparticle

SEM Analysis of the Synthesized Nanoparticles



e

Figures 4.2A-D present the SEM micrograph of the $Zn_{1-x}Sn_xO$ sample at x = 0, corresponding to undoped ZnO.

The SEM micrographs of $Zn_{1-x}Sn_xO$ samples A–D, corresponding to x=0.00, 0.001, 0.003 and 0.005, respectively, show that Sn incorporation modifies the surface morphology and particle aggregation. Undoped ZnO (sample A) consists of relatively large, irregular and strongly agglomerated particles with poorly defined boundaries. At x=0.001 (sample B), the particles become more clearly separated and exhibit distinct angular/irregular grains with noticeable interparticle voids. With further Sn addition (x=0.003, (sample C)), the morphology becomes finer and more agglomerated, while the highest Sn concentration (x=0.005 (sample D)) exhibits a comparatively compact and fine-grained surface texture. Overall, the SEM observations suggest that Sn doping affects nucleation and grain-growth processes, probably through lattice distortion and defect formation arising from substitutional incorporation of Sn ions. However, because the SEM images were recorded at different magnifications, a strict quantitative comparison of particle sizes should be avoided unless grain-size measurements are performed from images acquired at identical magnification.

The progressive changes in peak shape and relative intensity with Sn concentration indicate that Sn incorporation influences crystallinity, lattice strain and crystallite growth. These structural changes are consistent with the SEM results, where increasing Sn content produces noticeable modifications in particle morphology and aggregation. The combined SEM and XRD results therefore indicate that Sn doping mainly introduces microstructural distortion and modifies grain growth while preserving the fundamental ZnO wurtzite phase. These results are broadly consistent with recent studies on Sn-doped ZnO. Munna et al., (2023) reported that Sn incorporation preserved the wurtzite ZnO structure but produced diffraction-peak shifts, reduced crystallite size and increased lattice strain/dislocation density, while the FESEM images showed irregular and non-uniform particle morphologies. Similarly, Arif et al., (2025) reported that Sn doping retained the wurtzite structure but reduced crystallinity and altered the morphology toward more irregular and agglomerated particles because of dopant-induced lattice distortion and changes in crystal-growth kinetics. Thus, the present $Zn_{1-x}Sn_xO$ samples follow the general behaviour reported in the literature: low-level Sn doping does not destroy the ZnO crystal structure but significantly influences crystallite growth, defect formation, particle morphology and agglomeration.

The EDS analysis (as shown in Table 4.1 (A to D) and Figures 4.3 (A to D) of the $Zn_{1-x}Sn_xO$ sample at x = 0, corresponding to nominally undoped ZnO, confirms that Zn is the predominant element, with an atomic concentration of 78.67 at.% and a weight concentration of 83.64 wt.%. No Sn was detected, which is consistent with the nominal x = 0 composition. However, Fe (5.21

at.%), Mn (5.24 at.%), Ti (4.30 at.%) and Ca (5.06 at.%) were also detected, together with a small amount of carbon (1.50 at.%). These elements are not expected as constituents of pure ZnO and may originate from substrate contributions, precursor impurities, or contamination during film deposition. Similar substrate-related signals have been reported in EDS analyses of ZnO thin films, demonstrating that the measured elemental composition can include contributions from the substrate.

The EDX analysis of the undoped ZnO sample (x = 0.00) (Table 4.2A) shows that zinc (Zn) is the dominant detected element, with an atomic concentration of 78.67% and a weight concentration of 83.64%, confirming the Zn-rich nature of the sample. However, small amounts of Fe (5.21 at.%), Mn (5.24 at.%), Ti (4.30 at.%), Ca (5.06 at.%), and C (1.50 at.%) were also detected. These additional elements may originate from precursor impurities, contamination during sample preparation or handling, the substrate, or the experimental environment. Notably, Sn was not detected, which is consistent with the nominal composition of the undoped sample (x=0.00). Oxygen is also not listed in the quantitative results, which may be due to the limitations of the EDX measurement or the analytical conditions used. Overall, the EDX result confirms Zn as the major constituent of the undoped ZnO sample.

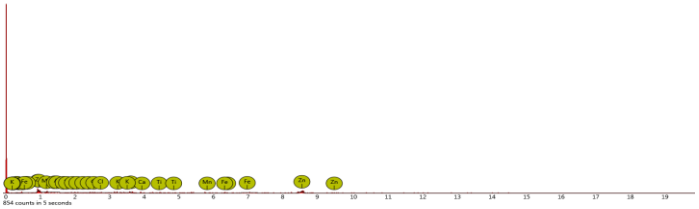


Figure 3A: EDS spectrum for sample A

Table 2A: EDS data for sample A

Element Number	Element Symbol	Element Name	Atomic Conc.	Weight Conc.
30	Zn	Zinc	78.67	83.64
26	Fe	Iron	5.21	4.74
25	Mn	Manganese	5.24	4.68
22	Ti	Titanium	4.30	3.35
20	Ca	Calcium	5.06	3.30
6	C	Carbon	1.50	0.29
12	Mg	Magnesium	0.00	0.00
19	K	Potassium	0.00	0.00
13	Al	Aluminium	0.00	0.00
14	Si	Silicon	0.00	0.00
15	P	Phosphorus	0.00	0.00
16	S	Sulfur	0.00	0.00
17	Cl	Chlorine	0.00	0.00

The EDX analysis of the $Zn_{1-x}Sn_xO$ sample (Table 4.1B and Figure 4.3 B) at (x = 0.001) confirms the presence of Zn and Sn, with Zn remaining the dominant metallic constituent at 51.85 at.% (69.91 wt.%), while Sn was

detected at 14.73 at.% (7.39 wt.%), indicating the successful incorporation of Sn into the sample. The detection of Sn distinguishes this sample from the undoped ZnO and is consistent with previous studies, where EDX analyses of Sn-doped ZnO similarly revealed the simultaneous presence of Zn, Sn, and O, with Sn concentration generally increasing as the nominal doping level increased (Oyewo et al., 2022). However, the relatively high measured Sn atomic concentration compared with the nominal doping level (x = 0.001) suggests that EDX quantification may not directly reflect the intended bulk stoichiometry, particularly because EDX is a localized, semi-quantitative technique and may be influenced by elemental distribution, surface effects, and matrix corrections. The presence of additional elements, including K, Ca, Fe, Al, Mn, Si, S, P, N, and Cl, may be attributed to impurities from the precursors, substrate, sample preparation, or environmental contamination. Overall, the EDX result supports the incorporation of Sn into the ZnO matrix, in agreement with existing reports on Sn-doped ZnO, although complementary techniques such as XPS or ICP-MS would provide more reliable confirmation of the actual Sn concentration.

Table 2B: EDS data for sample B

Element Number	Element Symbol	Element Name	Atomic Conc.	Weight Conc.
30	Zn	Zinc	51.85	69.91
50	Sn	Sn	14.73	7.39
19	K	Potassium	3.88	3.12
20	Ca	Calcium	3.76	3.11
26	Fe	Iron	2.52	2.90
13	Al	Aluminium	5.17	2.88
25	Mn	Manganese	2.10	2.38
14	Si	Silicon	3.74	2.17
16	S	Sulfur	2.56	1.69
15	P	Phosphorus	2.58	1.65
7	N	Nitrogen	5.41	1.56
17	Cl	Chlorine	1.69	1.24
22	Ti	Titanium	0.00	0.00
6	C	Carbon	0.00	0.00

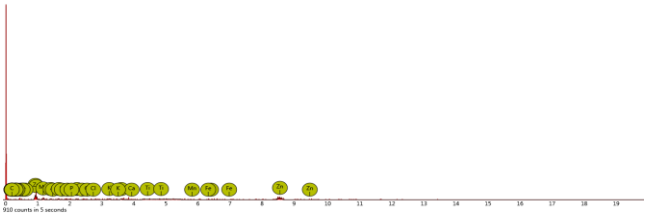


Figure 3B: EDS spectrum for sample B

The EDX analysis of the $Zn_{1-x}Sn_xO$ sample at x=0.003x = 0.003 shows that Zn remains the dominant constituent, with an atomic concentration of 55.94% and a weight concentration of 72.26%, while Sn is clearly detected at 19.68 at.% and 9.45 wt.%, confirming the successful incorporation of Sn into the ZnO material. Compared with the sample at x=0.001x = 0.001, the higher detected Sn concentration is consistent with the expected increase in Sn incorporation with increasing dopant concentration. This trend agrees with previous studies on Sn-doped ZnO, where EDX/EDS analysis confirmed the presence of Zn, O, and Sn in doped samples and generally showed an increase in the detected Sn content with increasing nominal Sn concentration. However, the measured Sn concentration is considerably higher than the nominal doping level, which may be attributed to the localized and semi-quantitative nature of EDX analysis, possible compositional inhomogeneity, surface enrichment, or matrix effects; therefore, the EDX values should not be interpreted as the exact bulk composition. The detection of minor amounts of Fe, Mn, Ti, Ca, K, N, Cl, and C may be associated with precursor impurities, substrate contributions, sample preparation, or environmental contamination. Overall, the EDX result confirms the presence and successful incorporation of Sn in the ZnO matrix, in agreement with existing reports on Sn-doped ZnO materials.

Table 2C: EDS data for sample C

Element Number	Element Symbol	Element Name	Atomic Conc.	Weight Conc.
30	Zn	Zinc	55.94	72.26
50	Sn	Sn	19.68	9.45
26	Fe	Iron	4.23	4.67
25	Mn	Manganese	3.22	3.49
22	Ti	Titanium	3.07	2.90
20	Ca	Calcium	3.05	2.41
19	K	Potassium	2.74	2.12
7	N	Nitrogen	4.93	1.37
17	Cl	Chlorine	1.27	0.89
6	C	Carbon	1.85	0.44
13	Al	Aluminium	0.00	0.00
14	Si	Silicon	0.00	0.00
15	P	Phosphorus	0.00	0.00
16	S	Sulfur	0.00	0.00

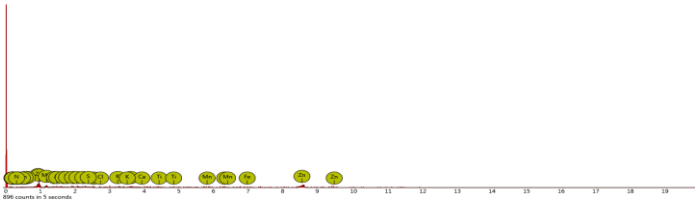


Figure 3C: EDS spectrum for sample C

Table 2D: EDS data for sample D

Element Number	Element Symbol	Element Name	Atomic Conc.	Weight Conc.
30	Zn	Zinc	51.94	67.09
50	Sn	Sn	23.68	11.03
26	Fe	Iron	5.09	5.05
25	Mn	Manganese	4.23	4.12
22	Ti	Titanium	3.21	3.03
20	Ca	Calcium	2.95	2.67
19	K	Potassium	2.43	2.14
7	N	Nitrogen	3.64	3.21
17	Cl	Chlorine	2.00	1.01
6	C	Carbon	0.83	0.60
13	Al	Aluminium	0.00	0.00
14	Si	Silicon	0.00	0.00
15	P	Phosphorus	0.00	0.00
16	S	Sulfur	0.00	0.00

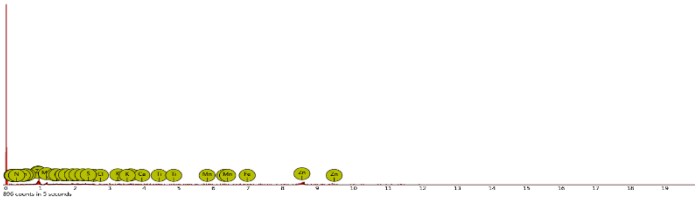


Figure 3D: EDS spectrum for sample D

Electrical Properties of Sn doped ZnO Films

Current – Voltage characteristics of Sn doped ZnO

Figure 4 presents the current–voltage (I–V) characteristics of $Zn_{1-x}Sn_xO$ samples with Sn concentrations of x = 0.000, 0.001, 0.003, and 0.005,

designated as Samples A, B, C, and D, respectively. The measurements were conducted over an applied voltage range of approximately −6 to +6 V. The I–V curves exhibit an approximately linear relationship between the applied voltage and the measured current, with the current increasing progressively as the applied voltage increases in both positive and negative directions. The curves also pass close to the origin, indicating negligible current at zero applied voltage. This behaviour suggests predominantly ohmic conduction within the investigated voltage range. However, slight deviations from ideal linearity are observable, which may be associated with variations in charge-carrier transport, microstructural defects, or contact resistance. The observed linear I–V characteristics are consistent with the findings of Humayun et al. (2013), who reported ohmic conduction in Sn-doped ZnO nanorods based on their approximately linear current–voltage curves.

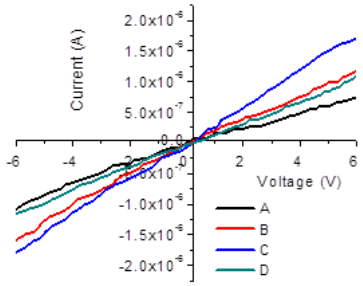


Figure 4: current–voltage (I–V) characteristics of $Zn_{1-x}Sn_xO$ samples with (A) x = 0.000, (B) 0.001, (C) 0.003, and (D) 0.005

A comparison of the samples reveals that Sample C exhibits the highest current response, reaching approximately 1.7×10^{-6} C at 6 V, whereas Samples A, B, and D exhibit comparatively lower current magnitudes. Sample C generally demonstrates the lowest current response, while Samples B and D exhibit intermediate values. This variation indicates that the electrical transport properties of the synthesized $Zn_{1-x}Sn_xO$ materials are influenced by Sn incorporation. Since electrical conductance is determined by the slope of the I–V curve, the relatively steeper slope of Sample A suggests higher conductance and lower resistance compared with the other samples. The reduction in current response observed in the Sn-containing samples may be associated with changes in carrier mobility, defect distribution, and grain-boundary resistance. Although Sn^{4+} incorporation into ZnO can potentially enhance electron concentration through donor-related effects, the resulting electrical conductivity depends on the combined influence of carrier concentration and mobility. This interpretation agrees with the findings of Yildiz et al. (2012), who demonstrated that electron transport in Sn-doped polycrystalline ZnO is strongly influenced by potential barriers and structural variations at grain boundaries.

The observed non-monotonic variation in current with Sn concentration suggests that the electrical response is not governed solely by the nominal dopant concentration. Rather, competing effects involving charge-carrier generation, defect formation, grain-boundary scattering, and microstructural changes may contribute to the measured conductivity. Similar concentration-dependent electrical behaviour has been reported in Sn-doped ZnO nanocrystalline materials, where resistivity initially decreased with Sn incorporation but increased at higher doping concentrations. The authors attributed the initial reduction in resistivity partly to the donor effect of Sn^{4+} ions substituting Zn^{2+} sites, while the subsequent increase was associated with changes in the material's electrical properties at higher dopant concentrations. Therefore, the present results demonstrate that Sn incorporation modifies the electrical transport characteristics of ZnO, although the undoped sample exhibits the highest current response under the measurement conditions employed. Further Hall-effect measurements and quantitative resistivity analysis are recommended to establish the contributions of carrier concentration and mobility to the observed electrical behaviour.

Effect of Sn Concentration on the Electrical Conductivity of $Zn_{1-x}Sn_xO$ Films

Figure 5 illustrates the variation of electrical conductivity with Sn concentration for the $Zn_{1-x}Sn_xO$ samples. The samples are designated A, B, C, and D, corresponding to nominal Sn concentrations of 0.000, 0.001, 0.003, and 0.005, respectively, as previously defined. The graph demonstrates a concentration-dependent variation in electrical conductivity, with an

initial increase followed by a decrease at higher Sn concentration.

The electrical conductivity increases from approximately 26 S cm^{-1} for Sample A to 36 S cm^{-1} for Sample B and reaches a maximum of approximately 51 S cm^{-1} for Sample C. However, a further increase in Sn concentration results in a reduction in conductivity to approximately 42 S cm^{-1} for Sample D. This indicates that Sn incorporation enhances the electrical conductivity of ZnO up to an optimum concentration, beyond which the conductivity decreases. Sample C therefore exhibits the highest measured conductivity among the investigated compositions, while Sample A exhibits the lowest.

The initial increase in conductivity observed in the present study can be attributed, in part, to the possible donor effect of Sn^{4+} ions incorporated into the ZnO lattice. Substitution of Zn^{2+} by Sn^{4+} may introduce additional electrons, thereby increasing the concentration of mobile charge carriers. This explanation is consistent with the findings of Haseman et al. (2018), who reported increased electrical conductivity and carrier concentration with increasing Sn incorporation in ZnO single crystals. Similarly, the study Influence of Sn Doping on the Optoelectronic Properties of ZnO Nanoparticles reported an increase in carrier concentration with Sn doping, although carrier mobility decreased as the doping level increased (Haseman et al., 2018).

The subsequent reduction in conductivity from approximately 51 S cm^{-1} in Sample C to 42 S cm^{-1} in Sample D suggests that excessive Sn incorporation may introduce competing effects that restrict charge transport. Possible mechanisms include increased ionized impurity scattering, structural defects, and grain-boundary resistance, which may reduce carrier mobility despite an increase in carrier concentration. This behaviour agrees with the findings of the 2013 study Structure–Property Correlation of Pure and Sn-Doped ZnO Nanocrystalline Materials Prepared by Co-precipitation, which reported an initial decrease in electrical resistivity with increasing Sn concentration, followed by an increase at higher doping levels. The authors attributed the initial improvement partly to the donor effect of Sn^{4+} ions (Verma et al., 2015).

Furthermore, Yildiz et al. (2012) demonstrated that electron transport in Sn-doped polycrystalline ZnO is strongly influenced by potential fluctuations and energy barriers at grain boundaries. These effects provide a possible explanation for the observed reduction in conductivity at the highest Sn concentration investigated in the present study.

Consequently, the conductivity enhancement up to Sample C, followed by a decline in Sample D, suggests a concentration-dependent balance between carrier generation] and carrier-scattering mechanisms. Within the investigated composition range, Sample C (x = 0.003) exhibits the highest measured electrical conductivity of approximately 51 S cm^{-1}.

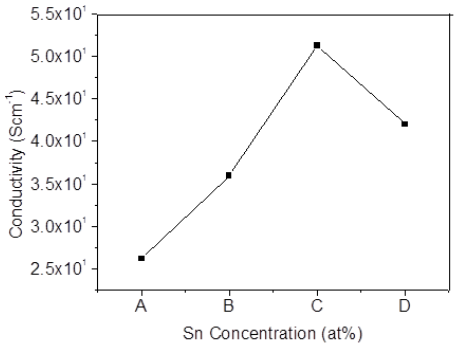


Figure 5: Electrical conductivity of Sn concentration for the $Zn_{1-x}Sn_xO$ samples

Electrical Resistivity versus Sn Concentration of Sn doped ZnO

Figure 6 depicting resistivity as a function of Sn (Sn) concentration typically illustrates how the incorporation of Sn dopant influences the electrical properties of the base material. A characteristic trend observed in many studies is an initial decrease in resistivity with increasing Sn concentration, followed by a plateau or even a slight increase at higher doping levels. This behavior can be interpreted in the context of carrier concentration and mobility.

When Sn is introduced into the host lattice, it commonly acts as a donor, substituting for a host cation and contributing free electrons to the conduction band (Saiman et al., 2010; Zheng et al., 2006). The initial decrease in resistivity is attributed to the sharp increase in carrier concentration resulting from these additional free electrons. This phenomenon has been widely reported in Sn-doped indium oxide (ITO) and Sn-doped

zinc oxide (SZO) thin films (Saiman et al., 2011; Li et al., 2010).

However, as the Sn concentration continues to increase beyond a certain threshold, the resistivity begins to rise. This effect is commonly attributed to reduced carrier mobility: Higher dopant concentrations can increase ionized impurity scattering, thereby reducing the mobility of charge carriers despite higher carrier concentrations, resulting in a net increase or stagnation in conductivity (Li et al., 2026).

This non-linear relationship is corroborated by Zheng et al. (2006) who observed that the resistivity of Sn-doped ZnO films decreased with Sn concentration up to 2 at.%, after which further increases in Sn content led to a slight rise in resistivity, attributed to a reduction in carrier mobility. Similarly, Li et al. (2010) reported the lowest resistivity at an optimal Sn doping level, beyond which the resistivity increased due to increased scattering and phase separation.

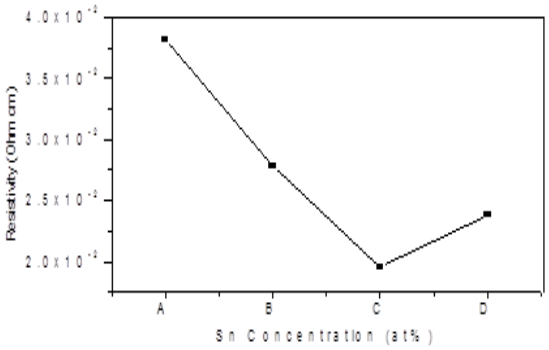


Figure 6: Electrical resistivity of Sn concentration for the $Zn_{1-x}Sn_xO$ samples

Optical Properties of Sn doped ZnO

Optical Transmittance Behaviour of Sn-doped ZnO

Figure 7 shows the optical transmittance spectra, recorded over 300–800 nm, of ZnO thin films doped with Sn at concentrations of 0.000 (sample A), 0.001 (sample B), 0.003 (sample C) and 0.005 (sample D). All four films exhibit the two characteristic regions of a wide-band-gap II–VI oxide semiconductor: a sharp fundamental absorption edge in the near-UV (below ~400 nm), where the transmittance collapses from its plateau value to below 20 %, and a high, relatively flat transmission plateau throughout the visible and near-infrared region. The spectra confirm that all samples retain the high optical quality required for transparent-conductor and optoelectronic applications. In the plateau region, the undoped film (sample A) is the most transparent, reaching ~98 %. On doping, the average visible transmittance decreases to ~94 % at 0.001 (sample B) and to a minimum of ~90 % at 0.003 (sample C), before partially recovering to ~95 % at 0.005 (sample D). This non-monotonic dependence of transmittance on Sn content is a frequently reported feature of doped ZnO systems.

Substitution of Zn^{2+} by Sn^{4+} introduces donor states and raises the free-carrier concentration; the associated free-carrier absorption and sub-gap defect absorption reduce transmittance, which accounts for the drop from samples A to C. Sn^{4+} acts as a double donor on the Zn^{2+} site, raising the free-electron concentration and pushing the Fermi level into the conduction band. The lowest conduction states become occupied and are no longer available for optical transitions, so the absorption edge shifts to higher photon energy (Rüzgar, 2025). The strong blue-shift of the 0.005 film (sample D) is consistent with it having the highest effective carrier concentration, and reproduces the classic Burstein–Moss signature.

At intermediate doping (0.001–0.003), the lattice is increasingly strained by the ionic-radius mismatch between Sn^{4+} (0.69 Å) and Zn^{2+} (0.74 Å), promoting smaller grains, higher grain-boundary density and greater surface roughness (Russiarani et al., 2023). All of these scatter visible light and lower the plateau, explaining why C (0.003) is the least transparent.

The partial recovery at 0.005 (D) suggests improved film homogeneity, possible solubility-limit effects (segregation of excess Sn to grain boundaries rather than the lattice), or a smoother surface morphology at this concentration.

All films show a steep absorption edge near 375–390 nm, confirming a direct allowed transition and good crystallinity. Reading the cut-off directly, the edges fall at approximately 380 nm (sample A), 390 nm (sample B), 390 nm (sample C) and 375 nm (sample D), so that the sample D is the most blue-shifted and the intermediate films (samples B and C) are the most red-shifted. Converting the cut-off to an optical band gap gives roughly 3.26 eV for sample A, ~3.18 eV for samples B and C, and ~3.31 eV for sample D. These values are confirmed using Tauc plot.

The spectral form of >90 % visible transmittance combined with a UV cut-off near 3.2–3.3 eV is the canonical fingerprint of ZnO-based films (Kumar & Das, 2026)

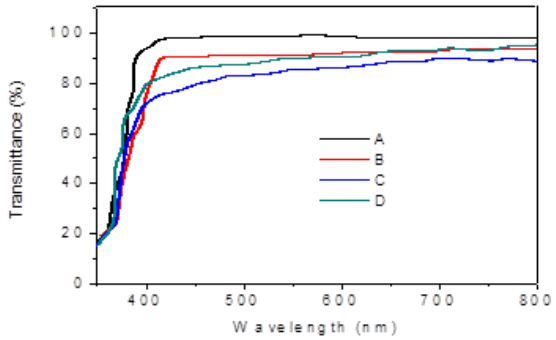


Figure 7: Transmittance against wavelength of Sn doped ZnO

Optical Absorption Coefficient of Sn-doped ZnO Films

Figure 8 shows the optical absorption coefficient (α) as a function of wavelength over 300–800 nm for ZnO thin films doped with Sn. All four films display the behaviour characteristic of a direct-band-gap semiconductor: a high absorption coefficient ($\alpha \approx 0.75$) in the near-UV, a steep absorption edge between ~360 and ~390 nm, and a low-absorption plateau extending across the visible region.

The undoped sample has the sharpest edge and most blue-shifted onset (370 nm), while the doped films show progressively red-shifted and more gradual edges, in the order A < B < D < C. Sample C (0.003) exhibits the most red-shifted onset and the most pronounced sub-edge tailing. Estimating the optical band gap from the absorption onset gives the largest gap for A (~3.35 eV) and the smallest for sample C, with samples B and D intermediate, so that the apparent band gap narrows on doping and is smallest at 0.003.

In the visible region (400–800 nm) the residual absorption follows the order C > D > B > A. The undoped film (A) is essentially non-absorbing ($\alpha \rightarrow 0$), whereas the doped films show a rising baseline absorption that increases to ~0.02 (B), ~0.05 (D) and ~0.08 (C). The absence of crossovers in the visible region establishes a clear, dopant-dependent hierarchy of sub-band-gap absorption.

The convergence of all curves to a high absorption coefficient below ~370 nm confirms that the fundamental optical transition in each film is governed by the ZnO host, whose room-temperature direct band gap of 3.2–3.4 eV is well established (Özgür et al., 2005; Srikant & Clarke, 1998). The ~3.35 eV onset of the undoped film (sample A) is fully consistent with this value and confirms the optical quality of the matrix.

The systematic red-shift and broadening of the absorption edge upon Sn incorporation (A < B < D < C) indicate a progressive narrowing of the optical band gap and an increase in band-edge disorder. Two coupled mechanisms account for this. First, substitution of Zn^{2+} by Sn^{4+} generates donor states and lattice strain owing to the ionic-radius mismatch between Sn^{4+} and Zn^{2+}; this promotes grain refinement, higher grain-boundary density and point-defect formation, all of which introduce localized states within the gap (Caglar et al., 2009; Ilican et al., 2008). Second, these defect and disorder states produce an exponential Urbach band-tail below the absorption edge, which manifests as the gradual edge and enhanced sub-edge absorption seen most strongly in sample C (Russiarani & Ramesh Kumar, 2023). The dominance of band-gap renormalization and band-tailing over the opposing Burstein–Moss widening at these doping levels explains the net narrowing of the gap, a competition documented for doped ZnO by Saw et al. (2015) and Kim et al. (2010). The slightly larger gap and lower tailing of the 0.005 film (sample D) relative to the 0.003 film (sample C) suggests improved lattice ordering or dopant segregation near the solubility limit, consistent with the non-monotonic optical behaviour reported for Sn-doped ZnO by Chahmat et al. (2012).

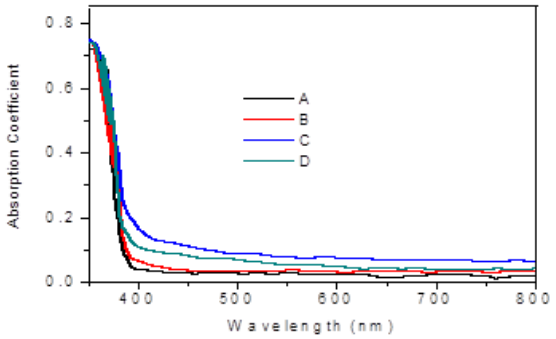


Figure 8: Plot of absorption coefficient against wavelength for Sn doped ZnO

Optical Band Gap (Tauc Analysis)

The optical band gap of each film was determined from the Tauc relation for a direct allowed transition, $(\alpha h\nu)^2 = A(h\nu - Eg)$, by plotSng $(\alpha h\nu)^2$ against photon energy hν and extrapolaSng the linear region of the absorption edge to $(\alpha h\nu)^2 = 0$. Figure 4.9 (a–d) shows the Tauc plots for the ZnO films doped with Sn at 0.000 (A), 0.001 (B), 0.003 (C) and 0.005 (D). In every case the plot exhibits a well-defined linear region near the absorption edge, confirming that the fundamental transition in these films is direct and allowed, as expected for ZnO.

The band gaps obtained from the tangent intercepts were 3.30 eV (A), 3.32 eV (B), 3.35 eV (C) and 3.32 eV (D). The band gap therefore widens progressively with Sn incorporation, reaching a maximum of 3.35 eV at a Sn content of 0.003 (C), and then contracts slightly to 3.32 eV at the highest content of 0.005 (D). The overall change is a blue-shift of up to 0.05 eV relative to the undoped film, followed by a small red-shift at the highest doping level. Table 4.3 summarizes the results.

Table 3: Optical band of Sn doped ZnO

Sample	Sn content	Optical band gap Eg (eV)	Shift vs. undoped
A	0.000	3.30	— (reference)
B	0.001	3.32	+0.02 (blue-shift)
C	0.003	3.35	+0.05 (blue-shift, max)
D	0.005	3.32	+0.02 (slight red-shift from C

The band gap of the undoped film (3.30 eV) is in excellent agreement with the accepted room-temperature direct gap of ZnO (3.2–3.4 eV) reported by Özgür et al. (2005), Srikant and Clarke (1998) and, more recently, Guillén (2025), who quotes ~3.4 eV for polycrystalline ZnO films. This confirms the optical quality of the host matrix and validates the Tauc extraction.

The widening of the gap on Sn incorporation is attributed primarily to the Burstein–Moss effect. Sn^{4+} substitutes for Zn^{2+} on the lattice (or occupies interstitial/vacant Zn sites) and acts as a double donor, raising the free-electron concentration so that the lowest conduction-band states become occupied and the apparent absorption edge shifts to higher photon energy (Burstein, 1954; Moss, 1954; Saw et al., 2015). This interpretation is strongly supported by recent work on the same system: Munna et al. (2023) reported that the optical band gap of ZnO increases with Sn content because Sn^{4+} substitutes Zn^{2+} in the lattice, and Russiarani and Ramesh Kumar (2023) likewise observed a slight increase in band gap with increasing Sn doping. A comparable Sn-induced blue-shift was reported by Rodríguez et al. (2023) for ZnO films with 1–3 at% Sn, and the combined experimental–theoretical study of Yildirimcan et al. (2024) on ZnO:Sn confirmed the donor role of Sn^{4+} and the associated band-gap engineering. The magnitude of the shift observed here (≤0.05 eV) is modest and of the same order as these recent reports, consistent with the low dopant concentrations used (≤0.005).

The slight contraction of the gap at the highest doping (0.005, from 3.35 to 3.32 eV) reflects the onset of competing band-gap renormalization and band-tailing. At higher carrier and defect densities, many-body electron–electron and electron–impurity interactions and Urbach band-tailing from structural disorder narrow the

gap and oppose the Burstein–Moss widening (Saw et al., 2015; Kim et al., 2010). This non-monotonic trend also agrees with the companion absorption-coefficient and transmittance measurements in this work, where the 0.005 film showed partial recovery of its optical behaviour relative to the intermediate compositions, pointing to improved lattice ordering or dopant segregation near the solubility limit.

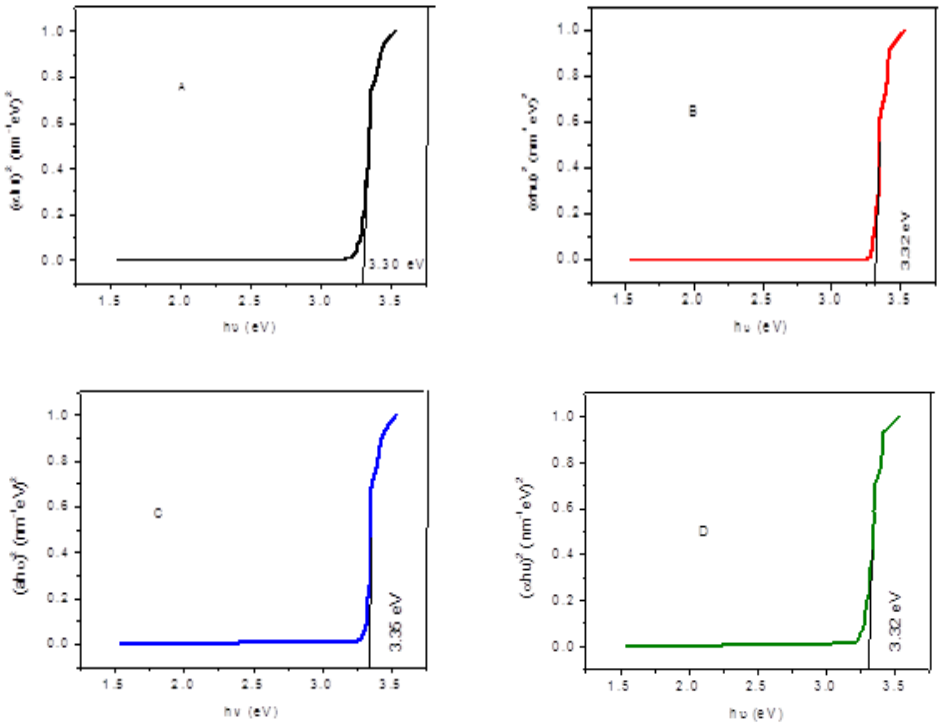


Figure 4.9: Optical bandgap Sn doped ZnO

CONCLUSION

The following conclusions are drawn from this study: No secondary SnO_2 or impurity phases were detected by XRD up to x = 0.005, confirming that Sn is incorporated substitutionally into the ZnO lattice. Sample C consistently exhibited the best overall properties across all characterization techniques — the largest crystallite size (20.47 nm), lowest microstrain (0.544%) and dislocation density (2.387×10^{-3} nm^{-2}), highest electrical conductivity (~51 S cm^{-1}), lowest resistivity, and widest optical band gap (3.35 eV). At x = 0.005 (Sample D), the crystallite size decreased, microstrain and dislocation density increased, electrical conductivity declined, and the band gap contracted slightly all indicative of the dopant concentration approaching the solubility limit, leading to enhanced lattice disorder, grain-boundary scattering, and defect formation. The sample with the best crystalline quality (largest crystallites, fewest defects) also exhibited the widest band gap, reinforcing the interpretation that crystallographic perfection governs the optical response. The Burstein–Moss effect is the dominant mechanism for band-gap widening at low Sn concentrations, while band-gap renormalization and Urbach band-tailing become significant at higher doping levels.

REFERENCES

Adelakun, O. D., Musa, A. Y., & Ahmed, U. (2020). Prospects of solar energy in Nigeria: A review. Journal of Sustainable Energy Engineering, 8(1), 45–55.

Altamura, G., Paire, M., Brémond, G., & Lincot, D. (2016). Optical properties of reactively sputtered Cu_2ZnSnS_4 solar absorbers determined by spectroscopic ellipsometry and spectrophotometry. Solar Energy Materials and Solar Cells, 149, 170–178. https://doi.org/10.1016/j.solmat.2016.01.014

Arif D, Khan R, Abid AY, Safeen K, Ali A, Amin MA, Akram K, Khan KH, Ali Z and Safeen A (2025). Influence of defects on the enhancement of thermoelectric properties in Sn-doped ZnO nanostructure synthesized via hydrothermal route. Front. Chem. 13:1598509. https://doi.org/10.3389/fchem.2025.1598509

Avasthi, S., & Agarwal, V. (2016). Recent advances in the development of ternary and quaternary semiconductor materials for optoelectronic applications. Journal of Materials Chemistry C, 4(25), 10265–10289. *https://doi.org/10.1039/C6TC01643J*.

Caglar, Y., Ilican, S., Caglar, M., & Yakuphanoglu, F. (2009). Effects of film thickness on the optical constants and microstructure of doped ZnO films. *Journal of Alloys and Compounds*, *466*(1–2), 311–317. *https://doi.org/10.1016/j.jallcom.2007.11.112*

Chahmat, N., Haddad, A., Ain-Souya, A., Ganfoudi, R., Attaf, N., Aida, M. S., & Ghers, M.
Chen, S., Yang, J.-H., Gong, X. G., Walsh, A., & Wei, S.-H. (2010). Intrinsic point defects and complexes in the quaternary kesterite semiconductor Cu_2ZnSnS_4. Physical Review B, 81(24), 245204. *https://doi.org/10.1103/PhysRevB.81.245204*

Green, M. A. (2003). Third generation photovoltaics: Advanced solar energy conversion. Springer. *https://doi.org/10.1007/978-3-662-04363-1*

Green, M. A. (2020). Photovoltaics and the global energy future. Progress in Photovoltaics: Research and Applications, 28(3), 243–249.

Green, M. A., Emery, K., Hishikawa, Y., Warta, W., & Dunlop, E. D. (2015). Solar cell efficiency tables (version 45). Progress in Photovoltaics: Research and Applications, 23(1), 1–9. *https://doi.org/10.1002/pip.2573*.

Guillén, C. (2025). Determination of the band gap energy of SnO_2 and ZnO polycrystalline films. *Micro*, *6*(1), 3. *https://doi.org/10.3390/micro6010003*

Haseman, M., Saadatkia, P., Warfield, J., Lawrence, J., Hernandez, A., Jellison, G. E., Boatner, L. A., & Selim, F. (2018). Optical and electrical properties of Sn-doped zinc oxide single crystals. Journal of Electronic Materials, 47(2), 1497–1504. *https://doi.org/10.1007/s11664-017-5942-6*

Ilican, S., Caglar, Y., Caglar, M., & Yakuphanoglu, F. (2008). Structural, optical and electrical properties of Sn-doped ZnO thin films. *Journal of Optoelectronics and Advanced Materials*, *10*(10), 2592–2598.

Kim, C. E., Moon, P., Kim, S., Myoung, J.-M., Jang, H. W., Bang, J., & Yun, I. (2010). Effect of carrier concentration on optical bandgap shift in ZnO:Ga thin films. *Thin Solid Films*, *518*(22), 6304–6307. *https://doi.org/10.1016/j.tsf.2010.03.042*

Kim, S., Yoon, J., & Kang, M. (2021). Zinc tin oxide thin films for optoelectronic devices. Journal of Alloys and Compounds, 872, 159623. https://doi.org/10.1016/j.jallcom.2021.159623

Kim, Y. J., & Lee, H. J. (2022). Optical and electrical properties of Zn-Sn-O films for transparent conducting electrodes. Journal of Materials Science: Materials in Electronics, 33(7), 4932–4941.

Kittel, C. (2005). Introduction to Solid State Physics (8th ed.). Wiley.
Li, X., Tan, F., Zhang, C., Zhou, J., Guo, Z., Yang, Y., Xie, Y., Cao, X., Feng, Y., Huang, C., Li, Z., Qu, Y., & Li, L. (2026). Research Progress on Transparent Conductive Properties of SnO_2 Thin Films. *CoaSngs*, *16*(1), 23. https://doi.org/10.3390/coaSngs16010023

Luque, A., & Hegedus, S. (Eds.). (2011). Handbook of photovoltaic science and engineering (2nd ed.). John Wiley & Sons. *https://doi.org/10.1002/9780470974704*

Mitzi, D. B., Gunawan, O., Todorov, T. K., Wang, K., & Guha, S. (2011). The path towards a high-performance solution-processed kesterite solar cell. Solar Energy Materials and Solar Cells, 95(6), 1421–1436. https://doi.org/10.1016/j.solmat.2011.01.005

Moss, T. S. (1954). The interpretation of the properties of indium antimonide. *Proceedings of the Physical Society. Section B*, *67*(10), 775–782. *https://doi.org/10.1088/0370-1301/67/10/306*

Munna, N., Abdur, R., Islam, R., Bashar, M. S. Farhad, S. F. U., Md. Kamruzzaman, Aziz, S., Md. Shaikh, A. A., Hossain, M., Jamal, M. S. (2023). Influence of Sn doping on the optoelectronic properties of ZnO nanoparticles. Nanoscale Adv. 5 (18): 4996–5004. *https://doi.org/10.1039/d3na00409k*

Nakamura, S., & Fasol, G. (1997). The Blue Laser Diode: GaN Based Light Emitters and Lasers. Springer.
Nid, A., & co-workers. (2026). Effect of Sn (Sn) doping on the properties of ZnO thin films prepared by solar spray pyrolysis. *Journal of Nano- and Electronic Physics*, *18*(2), 02038.

Nomura, K., Ohta, H., Takagi, A., Kamiya, T., Hirano, M., & Hosono, H. (2004). Room-temperature fabrication of transparent flexible thin-film transistors using amorphous oxide semiconductors. Nature, 432(7016), 488–492. *https://doi.org/10.1038/nature03090*.

Ohring, M. (2002). Materials Science of Thin Films: Deposition and Structure (2nd ed.). Academic Press.

Ohta, H., Kim, S. W., Mune, Y., Mizoguchi, T., Nomura, K., Ohta, S., ... & Hosono, H. (2008). Giant thermoelectric Seebeck coefficient of a two-dimensional electron gas in $SrTiO_3$. Nature Materials, 6(2), 129–134. https://doi.org/10.1038/nmat1821

Okoye, C. M. I., Nwosu, A. N., & Eze, F. U. (2021). Synthesis and characterization of ternary Zn–Sn–O thin films for solar applications. International Journal of Modern Physics B, 35(29), 2150273.

Oyewo, O. A., Ramaila, S., Mavuru, L., Onwudiwe, D. C. (2022). Enhanced photocatalytic degradation of methyl orange using Sn-ZnO/GO nanocomposite, Journal of Photochemistry and Photobiology, Vol. 11, 100131, *https://doi.org/10.1016/j.jpap.2022.100131*.

Özgür, Ü., Alivov, Y. I., Liu, C., Teke, A., Reshchikov, M. A., Doğan, S., AvruSn, V., Cho, S.-J., & Morkoç, H. (2005). A comprehensive review of ZnO materials and devices. *Journal of Applied Physics*, *98*(4), 041301. *https://doi.org/10.1063/1.1992666*

P. Würfel,.Physics of Solar Cells: From Principles to New Concepts", Wiley-WCH, Weinheim, (2005).
Rodríguez, I., & co-workers. (2023). Optical and structural properties of Sn-doped ZnO thin films. *MRS Advances*, *8*, 1434–1439. *https://doi.org/10.1557/s43580-023-00674-3*

Russiarani, S., & Ramesh Kumar, V. (2023). Structural and optical properties of Sn-doped zinc oxide (ZnO) thin films. *Iranian Journal of Chemistry and Chemical Engineering*, *42*(9).

Russiarani, S., Krishnaraj, S & Shanmugavadivelu, C. M. (2023). Structural and Optical Properties of Sn Doped Zinc Oxide (ZnO:Sn) Thin Films Prepared by Spray Pyrolysis Method, Iran. J. Chem. Chem. Eng., Vol. 42, No. 2, 449-460

Rüzgar, S. (2025). Enhanced Optoelectronic Properties of Zn-Doped SnO2 Thin Films Prepared by Nebulizer Spray Method, MAUN J. of Sci., 13(2), 357-363. *https://doi.org/10.18586/msufbd.1762798*

Saiman, S. A., Hazza, S. Q & Abbas, S. J (2026). Effect of Sn Doping on Structural and Electrical Properties of ZnO Thin Films Prepared by Chemical Spray Pyrolysis Method, Invention Journal of Research Technology in Engineering & Management (IJRTEM), 1(9), 1-5.

Saiman, S., Kumar, S., & Saiman, A. (2010). Effect of Sn doping on the structural and electrical properties of ZnO thin films. *Materials Chemistry and Physics*, 123(2-3), 398-403.

Sato, Y., Sano, K., Okamoto, K., & Niwa, H. (2012). Structural and electrical properties of Zn–Sn–O films prepared by RF sputtering. Thin Solid Films, 520(12), 4241–4246. https://doi.org/10.1016/j.tsf.2012.02.013

Saw, K. G., Aznan, N. M., Yam, F. K., Ng, S. S., & Pung, S. Y. (2015). New insights on the Burstein–Moss shift and band gap narrowing in indium-doped zinc oxide thin films. *PLoS ONE*, *10*(10), e0141180. *https://doi.org/10.1371/journal.pone.0141180*

Scragg, J. J., Dale, P. J., Peter, L. M., Zoppi, G., & Forbes, I. (2011). New routes to sustainable photovoltaics: Cu_2ZnSnS_4 thin films via co-electrodeposition. Physica Status Solidi (b), 248(9), 2039–2042. *https://doi.org/10.1002/pssb.201147146*.

Seo, J., & Yoo, H. (2022). Zinc–tin oxide film as an earth-abundant material and its versatile applications to electronic and energy materials. Membranes, 12(5), 485. *https://doi.org/10.3390/membranes12050485*

Smets, A. H. M., Jäger, K., Isabella, O., van Swaaij, R. A. C. M. M., & Zeman, M. (2016). Solar cell fundamentals: Technology and system applications. Cambridge University Press. https://doi.org/10.1017/CBO9781107476085

Srikant, A. V., & Clarke, D. R. (1998). On the optical band gap of zinc oxide. *Journal of Applied Physics*, *83*(10), 5447–5451. *https://doi.org/10.1063/1.367375*

Wang, T., Li, X., & Xu, J. (2018). Sputtering deposition of Zn–Sn–O thin films and their applications in photovoltaics. Materials Letters, 228, 191–195.

Yildirimcan, S., Erat, S., CeSnkaya, S., & Aycibin, M. (2024). A combined theoretical and experimental study on vertically aligned ZnO and ZnO:Sn. *Physics Letters A*, *516*, 129640. *https://doi.org/10.1016/j.physleta.2024.129640*

Yildiz, A., Serin, T., Öztürk, E., & Serin, N. (2012). Barrier-controlled electron transport in Sn-doped ZnO polycrystalline thin films. Thin Solid Films, 522, 90–94. *https://doi.org/10.1016/j.tsf.2012.09.006*

Zheng, B.J., Lian, J.S., Zhao, L. & Jiang, Q. (2011). Optical and electrical properties of Sn-doped CdO thin films obtained by pulse laser deposition, Vacuum, 85(9), 861-865, *https://doi.org/10.1016/j.vacuum.2011.01.002*.